Università degli Studi di Padova

Dipartimento di Fisica e Astronomia "Galileo Galilei"
Corso di Laurea Magistrale in Fisica

Fusion Hindrance and Pauli Blocking in ^{58}Ni + ^{64}Ni

Laureando:
Mirco Del Fabbro

Relatore:
Prof.ssa Giovanna Montagnoli
Correlatore:
Prof. Alberto Stefanini

Anno accademico 2018/2019

Contents

Chapter 1

Introduction

Heavy-ion fusion is a quite complex phenomenon whose study has been involving several experimental and theoretical efforts, after large Tandem electrostatic accelerators have been put into operation, and have allowed to produce medium-mass heavy-ion beams with sufficient energy to overcome the Coulomb barrier in collisions with targets of nearly all elements. A specific interest in the study of the fusion dynamics evolved in the seventies, following the awareness that fusion reactions between heavy stable nuclei can produce exotic nuclei away from stability on the proton-rich side of the mass valley and they are crucial for the synthesis of very heavy elements.

Measured fusion excitation functions of light heavy-ion systems essentially follow the predictions of the well-known Wong formula based on the quantal penetration of the barrier [1], but experimental and theoretical studies on near- and sub-barrier heavy-ion fusion received a strong push in the late 70's because two basic kinds of experimental evidences were discovered: on one side, experimenters found the first hints of generalised very large enhancements of cross sections with respect to the simple predictions of the Wong formula. On the other side, shortly after, measurements gave evidence of strong isotopic effects, that is, fusion excitation functions of near-by systems may differ substantially in magnitude and shape. This indicated that a close connection exists between the sub-barrier fusion dynamics and the low-lying collective structure of the two colliding nuclei, and the coupled-channels (CC) model was developed in order to reproduce the experimental evidences. In the following decade several experiments were performed aiming at clarifying this link in various experimental situations. Subsequently, Neil Rowley suggested [2] that the fusion barrier distributions (BD) originated by channel couplings could be obtained from the second derivative of the energy-weighted excitation functions with respect to the energy, and a second sequence of measurements started in the early 90's, aiming at extracting the shape of the BD for several different systems, as a fingerprint of channel couplings in the various cases. Measurements of this kind are very delicate and are still being performed nowadays. Around ten years later, an experiment performed at Argonne

Nat. Lab. [3] indicated that fusion cross sections of ^{60}Ni + ^{89}Y have an unexpected behaviour far below the barrier, i.e., they drop much faster than predicted by standard CC calculations. This opened a new area of research, and this phenomenon (named "hindrance") was soon recognised as a general effect, even if with different aspects whose origin is still a matter of debate and research in the community.

1.1 Physical motivation and choice of the system

The work of this thesis is based on a measurement of deep sub-barrier fusion of ^{58}Ni + ^{64}Ni.

The early experiments on fusion of Ni + Ni systems are well-known and indicated for the first time the possible influence of transfer reactions on near- and sub-barrier cross sections.

The cross sections of ^{58}Ni + ^{64}Ni decrease much slower with decreasing energy below the Coulomb barrier with respect to the ^{64}Ni + ^{64}Ni and ^{58}Ni + ^{58}Ni systems. Shortly after [4], this was associated with the availability, only in this system, of neutron transfer channels with positive Q-values. Later measurements for ^{58}Ni + ^{64}Ni confirmed the shape of the excitation function, but did not extend below 0.1 mb.

In many systems (like ^{64}Ni + ^{64}Ni and ^{58}Ni + ^{58}Ni), at deep sub-barrier energies, the cross section decreases very rapidly, so that the excitation function is much steeper than the prediction of standard coupled-channels (CC) calculations. This phenomenon was called fusion hindrance.

The system ^{40}Ca+^{96}Zr has a behaviour similar to ^{58}Ni + ^{64}Ni, because the slope of the sub-barrier excitation function is not so steep as for other Ca + Zr combinations, and this has been attributed to couplings with positive Q-value transfer channels. The excitation function of ^{40}Ca+^{96}Zr has been actually measured down to $\sim 2\mu$b with a regular trend of the cross sections not evidencing any sign of hindrance effect. Misicu and Esbensen [5] proposed the so called sudden approach, where a double folding potential is adopted (M3Y+repulsion), having a shallow pocket originating from the incompressibility of nuclear matter. This CC model has been quite successful in reproducing the hindrance behavior in a number of cases.
The CC analyses were performed in order to better understand the influence of transfer on the fusion of ^{40}Ca+^{96}Zr. Multi-phonon excitations were included in the coupling scheme, and the one- and two-nucleon transfer form factors were calibrated so that the existing data for neutron and proton transfer channels are reproduced by the CC calculations. In this way, the sudden CC model gives an excellent account of the fusion data.

This suggests that, since the Q-values for nucleon transfer are large and positive, the valence nucleons can flow more freely from one nucleus to the other without being hindered by Pauli blocking and therefore that should also occur in reactions of other heavy-ion systems with large positive Q-values for transfer.

The ^{58}Ni + ^{64}Ni system has a positive Q-value (+3.9 MeV) for 2 neutron pick-up therefore this thesis aims to the measurement of fusion cross section of this system down to $\sim 1\mu$b to check the presence of hindrance and compare it with the symmetric case ^{64}Ni + ^{64}Ni where hindrance has been clearly identified, and with the system ^{40}Ca + ^{96}Zr whose behaviour is similar to ^{64}Ni + ^{64}Ni. The possible influence of the Pauli exclusion principle will also be discussed.

Chapter 2

Sub-barrier fusion

2.1 Unidimensional and coupled-channel model

A first approach to the heavy-ion fusion reactions is within a unidimensional model in which the projectile and target nuclei are treated as being structureless. Under this condition, the potential is a function of only the relative distance r between the colliding nuclei and it consists of two components: the nuclear potential $V_N(r)$ and the Coulomb potential $V_C(r)$. The Coulomb potential is expressed as the electrostatic potential between two point-like charged particles placed at a distance r:

$$V_C(r) = \frac{e^2 Z_p Z_t}{4\pi\varepsilon r}$$

where Z_p and Z_t are respectively the projectile and target atomic number. The nuclear potential can be estimated in several ways. The ion-ion potential that has been widely used is the phenomenological Woods-Saxon potential:

$$V_N(r) = \frac{-V_0}{1 + e^{(r-R_0)/a_0}}$$

where R_0 is the radius, V_0 is the depth and a_0 is the diffuseness of the potential. The three parameters of the Woods-Saxon potential can be estimated by a set of empirical formulae obtained from the analysis of elastic scattering:

$$R_p = (1.2A_p^{1/3} - 0.09)fm \qquad R_t = (1.2A_t^{1/3} - 0.09)fm$$

$$R_0 = R_p + R_t$$

$$\gamma = 0.95\left(1 - 1.8\frac{A_p - 2Z_p}{A_t}\frac{A_t - 2Z_t}{A_p}\right)$$

$$V_0 = 16\pi\gamma a_0 \frac{R_p R_t}{R_p + R_t}$$

$$a_0 = \frac{1}{1.17[1 + 0.53(A_p^{-1/3} + A_t^{-1/3})]}$$

This empirical potential is called Akyuz-Winther potential [6]. The nuclear potential constructed in this way has been successful in reproducing experimental angular distributions of elastic and inelastic scattering for many systems.

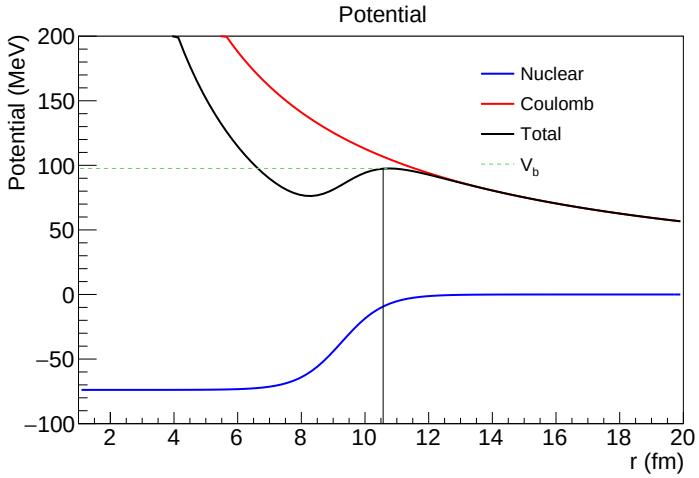

Figure 2.1: Unidimensional potential for the system ^{58}Ni+^{64}Ni: the red line represent the Coulomb potential, the blue one the nuclear potential and the black one the total potential.

The fusion of two spherical colliding nuclei can be described by the Schrödinger equation, as follows:

$$\left(-\frac{\hbar^2}{2\mu}\nabla^2 + V(r) - E\right)\Psi(r) = 0$$

where μ is the reduced mass of the system and V(r) the total potential. Since the nuclei involved are considered structureless V(r) is still the sum of the Coulomb potential and the nuclear potential. The solution of the equation can be expanded in terms of spherical harmonics, where the radial part obeys the following equation:

$$\left(-\frac{\hbar^2}{2\mu}\frac{d^2}{dr^2} + \frac{l(l+1)\hbar^2}{\mu r^2} + V(r) - E\right)u(r) = 0$$

In the last equation the centrifugal repulsive potential appears.

In this model the cross section is linked to the probability that the nuclei to overcome the barrier so that fusion may occur. Neglecting the spin, this probability is expressed by the transmission coefficient T_l(E) relative to the energy E and the partial wave l. The cross section is proportional to the transmission coefficient

$$\sigma_l(E) = \pi\lambda\!\!\!^{-2}(2l+1)T_l(E)$$

The total cross section is obtained by the sum over the partial waves, but not all the partial waves take part in fusion process, there is a maximum value of the angular momentum (l_{max}) above which fusion doesn't occur and the two nuclei separate after a period of contact. The fusion cross section is therefore:

$$\sigma_l(E) = \sum_0^{l_{max}} \pi\lambda\!\!\!^{-2}(2l+1)T_l(E)$$

The transmission coefficient can be obtained approximating the Coulomb barrier with a parabola. Within this approximation the transmission coefficient results to be:

$$T_l = \frac{1}{1 + e^{\frac{2\pi}{\hbar\omega_l}(V_{bl}-E)}}$$

where V_{bl} is the height of the barrier and ω_l is linked to the curvature of the parabola for the l^{th} wave. By assuming that the position of the barrier R_{bl} and ω_l are independent of the angular momentum the dependence of the transmission coefficient on the angular momentum, can be well approximated by shifting the incident energy by a rotational term:

$$T_l = T_0\left(E - \frac{\hbar^2 l(l+1)}{2\mu R_b^2}\right)$$

Using this transmission coefficient in the cross section equation and replacing the sum by an integral the fusion cross section results to be the Wong formula [1]:

$$\sigma_{fus}(E) = \frac{\hbar\omega_0 R_b}{2E} ln\left[1 + e^{\frac{2\pi}{\hbar\omega_0}(E-V_b)}\right]$$

The single barrier penetration model has achieved great success in the description of fusion cross section in light systems. On the contrary, it underestimates the sub-barrier fusion for heavier systems, although it reproduces the experimental data above the Coulomb barrier. This suggested that other degrees of freedom take part in the fusion process besides the relative motion of the two nuclei, for this reason it is necessary the coupled-channels model.

In the coupled-channels model it is necessary to consider the coupling between the relative motion and a nuclear intrinsic motion ζ, in this way the Hamiltonian becomes:

$$H(r,\zeta) = H_0(\zeta) + H_k(r) + V_l(r) + V_{int}(r,\zeta)$$

Where $H_k(r)$ is the kinetic energy and k the wave number, $V_l(r)$ is the ion-ion potential for the wave l, $H_0(\zeta)$ describes the internal structure of the two nuclei and V_{int} is the

coupling term.
With this Hamiltonian the stationary Schrödinger equation becomes:

$$\left(-\frac{\hbar^2}{2\mu}\frac{d^2}{dr^2}+\frac{l(l+1)\hbar^2}{\mu r^2}+V(r)-E\right)\Psi(r,\zeta)=-\left(H_0(\zeta)+V_{int}(r,\zeta)\right)\Psi(r,\zeta)$$

Denoting $\mid n>$ as the eigenstates and ε_n the eigenvalues of the intrinsic Hamiltonian $H_0(\zeta)$, the function $\Psi(r,\zeta)$ can be expanded in this eigenstates:

$$\Psi(r,\zeta)=\sum_n \chi_n(r)\mid n>$$

We have therefore a set of coupled differential equations and taking advantage of the orthonormality of the base of the eigenstates $\mid n>$, it is possible to apply the bra $<m\mid$ to the equations and obtain a new set of coupled equations whose solutions are the wave functions $\chi_n(r)$ of the relative motion of the two nuclei:

$$\left(-\frac{\hbar^2}{2\mu}\frac{d^2}{dr^2}+\frac{l(l+1)\hbar^2}{\mu r^2}+V(r)-E\right)\chi_m(r)=-\sum_n M_{mn}\chi_n(r)$$

where the coupling matrix M_{mn} has been defined as:

$$M_{mn}=\varepsilon_m\delta_{mn}+<m\mid V_{int}(r,\zeta)\mid n>$$

The matrix M_{mn} is symmetric and can be diagonalized using some appropriate approximations [7] [8].

In heavy-ion fusion reactions the so called incoming wave boundary condition (IWBC) is often applied. IWBC corresponds to the case where there is strong absorption within the inner region of the potential, so that the incoming flux never returns back. Other approximations are applied to reduce the dimension of the coupling matrix. In the coupled channel method, an excited state of internal spin I generates $I+1$ channels when it is coupled to the angular momentum l_i of the relative motion, since each orbital angular momentum of the type $l_i'=\mid l_i-I\mid,..,\mid l_i+I\mid$ satisfies the condition $\mathbf{J}=\mathbf{I}+\mathbf{l_i}$. The so called isocentrifugal approximation reduces the number of channels by assuming that the orbital angular momentum is the same in all reaction channels, under this condition there is only one channel for each excited state (instead of I+1). It can be also assumed that it is possible to factorize the coupling potential in two terms which depend separately on the intrinsic and relative motions

$$<m\mid V_{int}(r,\zeta)\mid n>=F(r)<m\mid G(\zeta)\mid n>$$

Another approximation is based on supposing $F(r)=F(R_b)$ constant where $F(R_b)$ is the value of F at the barrier (constant coupling approximation). This approximation

is not used by CCFULL, the program employed in this thesis for the cross section calculation). Under this condition the coupling matrix can be diagonalized by a unitary matrix U:

$$Y_m = \sum_n U_{mn}\chi_n \qquad \sum_{ij} U_{ni}M_{ij}U_{jm} = \delta_{mn}\lambda_m$$

What is obtained is a set of decoupled equations:

$$\left(-\frac{\hbar^2}{2\mu}\frac{d^2}{dr^2} + V(r) + \lambda_m F - E\right) Y_m(r) = 0$$

where the total potential for each channel becomes $V(r)+\lambda_m F$: in this way the single Coulomb barrier has been replaced with a set of barriers, each one with a transmission coefficient. The total transition coefficient can be obtained as the weighted sum of the transmission coefficients of each barrier.

$$T = \sum_m |U_{m1}|^2 T[E, V(r) + \lambda_m]$$

The factor $W_m = |U_{m1}|^2$ represents the contribution of the m-th barrier to the total fusion cross section that is therefore expressed as the weighted sum of the cross section of each barrier

$$\sigma^f = \sum_m W_m \sigma_m^f$$

2.2 Enhancement

The coupled-channel model leads to an enhancement of the fusion cross section. To understand how the model works a simple example with only two channel can be considered. Assuming a constant form factor F and a Q-value Q for the coupled channel, the coupling matrix is $M = \left(\begin{smallmatrix} 0 & F \\ F & -Q \end{smallmatrix}\right)$; then the decoupled equations for the present case are:

$$\left(-\frac{\hbar^2}{2\mu}\frac{d^2}{dr^2} + V(r) - E + \lambda_+ F\right) Y_+(r) = 0 \quad \left(-\frac{\hbar^2}{2\mu}\frac{d^2}{dr^2} + V(r) - E + \lambda_- F\right) Y_-(r) = 0$$

where $\lambda_\pm$ are the eigenvalues and $Y_\pm$(r) the eigenfunctions of the diagonalized coupling matrix. The eigenvalues of M and their weights turn out to be:

$$\lambda_\pm = \frac{-Q \pm \sqrt{Q^2 + 4F^2}}{2} \qquad P_\pm = \frac{F^2}{F^2 + \lambda_\pm^2}$$

In this way the barrier splits in two barriers, one higher by an amount λ_+ and one lower by λ_- than the original barrier. As shown in Fig.2.2 the transition probability

is increased for energies lower than and reduced for energies higher than the Coulomb barrier.

The effect of the enhancement is that of increasing the fusion cross section below

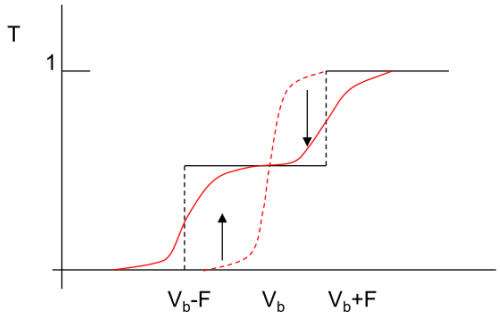

Figure 2.2: Comparison between transmission coefficient for unidimensional model (dashed red line) and coupled-channel model (solid red line), the step function (black line) is obtained in the classical limit

the Coulomb barrier as shown in Fig. 2.4.

2.3 Effect of transfer channel with positive Q-value

Recent studies have shown the influence of transfer processes with positive Q-value on the fusion reactions at sub-barrier energies, where an enhancement of the cross sections is observed with respect to the coupled channel calculations including the coupling to the vibrational and rotational states. The pair-transfer between the ground states of the interacting nuclei can be included in the coupled channel calculations through the introduction of a macroscopic form factor [9]

$$F_{trans}(r) = F_t \frac{dV_N^{(0)}}{dr}$$

where F_t is the coupling strength. An example of this phenomenon can be found in the ^{40}Ca+^{96}Zr system [10] where, as shown in Fig.2.3, the theoretical prediction underestimates the experimental data and there is no indication for the fusion hindrance effect.

2.4 Hindrance phenomenon

The experimental data of many systems (like ^{64}Ni+^{64}Ni) showed that, although the coupled-channels approach resulted successfully in reproducing the excitation function

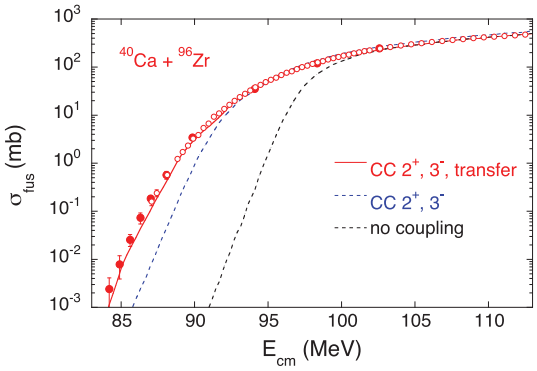

Figure 2.3: Fusion excitation function for the ^{40}Ca+^{96}Zr system

for heavy ion reactions at energies above and below the barrier, the experimental cross sections at far sub-barrier energies were overestimated. We also see that that the theoretical prediction overestimates the data at far sub-barrier energies. This phenomenon is called hindrance.

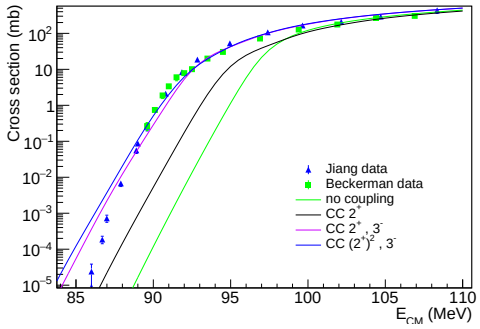

Figure 2.4: Comparison between ^{64}Ni+^{64}Ni experimental cross sections and theoretical prediction for unidimensional model (green line), coupled-channel model involving one phonon in the 2^+ excited states (black line),one phonon in the 2^+ and one in the 3^- excited states (violet line) and two phonon in the 2^+ excited states and one in the 3^- excited states (blue line).

In order to describe the hindrance a model has been proposed by Misicu and Esbensen in the sudden approach, that treats the nuclear density as frozen during the collision, assuming in this way that fusion occurs rapidly. They suggest that the incompressibility of nuclear matter becomes effective at small internuclear distances, thus generating a repulsive core in the ion-ion potential, which is then much shallower than standard potentials. This reduces the fusion probability. Hindrance shows up in different ways for different systems, so that to evidence its presence the logarithmic derivative of $E\sigma$ L(E) and the astrophysical factor S(E) are used. L(E) represents

the slope of the excitation function

$$L(E) = \frac{dln(E\sigma)}{dE} = \frac{1}{E\sigma}\frac{d(E\sigma)}{dE}$$

Where E is the energy in the center of mass of the system, L(E) increases with decreasing energy (Fig.2.5 left). The astrophysical factor S(E) is defined as:

$$S(E) = E\sigma(E)e^{2\pi\eta}$$

where η is the Sommerfeld parameter $\eta = 0.157 Z_p Z_t \sqrt{\frac{\mu}{E}}$ and μ is the reduced mass of the system.

The astrophysical factor is extracted directly from the excitation function (unlike L(E)), for this reason is a useful way to represent the trend of the excitation function for energies far below the Coulomb barrier (Fig.2.5 right). The two quantities S(E) and L(E) are related since

$$\frac{dS(E)}{dE} = S(E)(L - \frac{\pi\eta}{E})$$

therefore S(E) develops a maximum at the energy where the slope L is equal to:

$$L_{CS} = \frac{\pi\eta}{E}$$

That energy is conventionally taken as the threshold for deep sub-barrier hindrance.

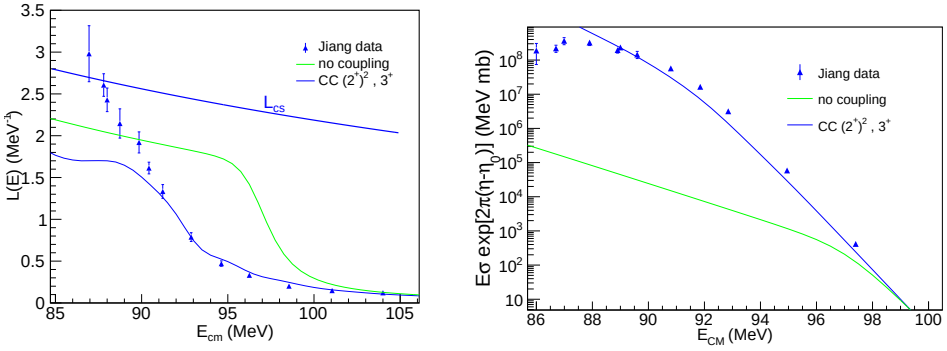

Figure 2.5: Logarithmic derivative (left) and astrophysical factor (right) for the ^{64}Ni+^{64}Ni system confronted with the theoretical prevision. Can be seen that the experimental value of L(E) overcome the L_{CS} value and S(E) present a maximum and as consequence the excitation function present hindrance (Fig.2.4)

Moreover, in some systems (like ^{58}Ni+^{64}Ni) where the analysis of the S factor does not show the presence of hindrance, this can be ascribed to the presence of transfer channels with positive Q-value.

Chapter 3

Set-up and experimental procedure

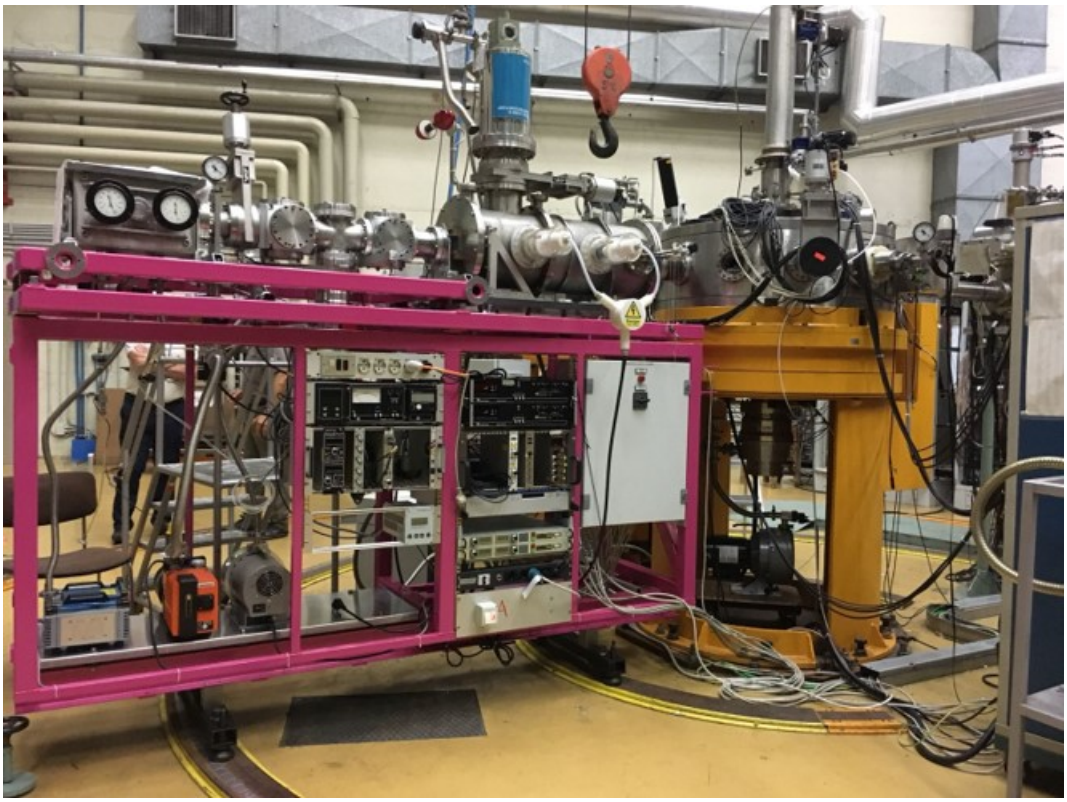

Figure 3.1: The Pisolo set-up

Fusion cross sections can be experimentally determined by direct detection of evaporation residues (ER) For this experiment the electrostatic deflector PISOLO (Fig. 3.2) has been used. This set-up has been designed to allow a fast and reliable measurement of relative and absolute fusion cross sections. The apparatus consists

of a reaction chamber, an electrostatic deflector and an energy, energy loss and time of flight telescope based on micro-channel plates, an ionization chamber and a silicon surface barrier detector.

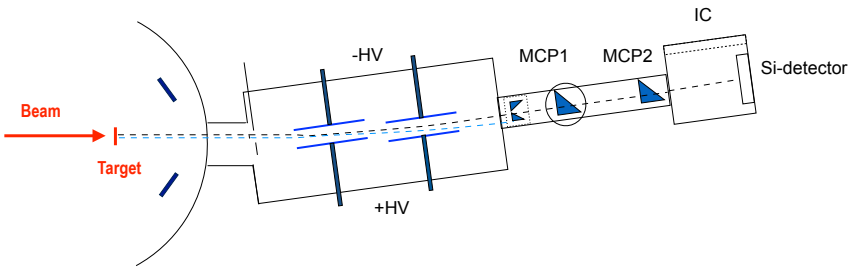

Figure 3.2: Scheme of the set-up

3.1 Scattering chamber and electrostatic deflector

The reaction chamber is made of stainless steel and has a cylindrical structure with an internal radius of 50 cm. One of its main properties is to allow a rotation keeping the vacuum inside (10^{-6} mbar) by means of a sliding seal, so to perform angular distribution measurements. Targets are fixed in a six-position holder (Fig.3.3 left) and consisted of 50 μg/cm^2 ^{64}Ni on a 20 μg/cm^2 carbon backing facing the beam. One of the positions is reserved for a quartz plate with a small central hole (1.5 mm in diameter), used to focus the beam. The target support is attached to the upper cover of the reaction chamber, and is moved through an external control system, so to be able to focus the beam at each change of energy and to change the target or its angle with respect to the beam direction.
Four 50 mm^2 silicon detectors are placed at the distance of 195 mm from the target, they are mounted on a circular support, to a detection angle of $\theta_{lab} = 16.05°$ with respect to the beam line, they are shown in Fig.3.3 (right). These detectors are used for the measurement of the Rutherford scattering cross section in order to normalize the fusion yields and to monitor the changes in beam position on the target, usually associated with the effects of the magnets installed on the beam line upstream of the reaction chamber. The monitor detectors have collimators with a diameter of 1.5 mm to reduce the counting rate and consequently the radiation damage. Taking into account that the surface of the detectors is not perpendicular to the line connecting each of them to the target, the total calculated solid angle is $\Delta\Omega_{mon}$=(166.7±1.7) μsr for the four monitors.

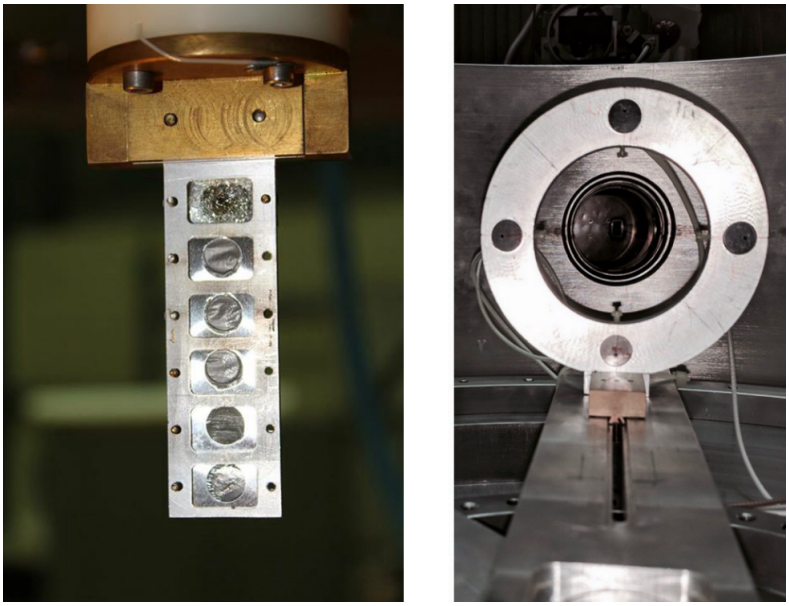

Figure 3.3: target holder(left) four monitor (right)

The electrostatic deflector allows the separation between the ER and the residual beam. The deflector exploits the difference in electrical rigidity between the ER and the particles of the transmitted beam. This rigidity is defined as $\eta = \frac{E}{q}$, where E is energy and q is the ion charge state. The deflector is placed at an angle of 4.7° with respect to the beam direction. The trajectory of charged particles in the electrostatic field region can be approximated to an arc of circumference, with radius of curvature r given by:

$$\frac{mv^2}{r} \sim q\varepsilon$$

where v and m are the velocity and mass of the ion respectively, while ε is transverse electric field. Given that for the momentum conservation law the momentum of ER and beam particles are approximately equal, the ratio between the radii of curvature of the residues (r_{ER}) and of the beam particles (r_b) is proportional to the respective electrical rigidities.

$$\frac{r_{ER}}{r_b} = \frac{(mv^2)_{ER}}{q_{ER}} \cdot \frac{q_b}{(mv^2)_b} \sim \frac{E_{ER}}{q_{ER}} \cdot \frac{q_b}{E_b} \sim \frac{m_b}{m_{ER}} \cdot \frac{q_b}{q_{ER}}$$

Since mass and charge state of the residues are usually greater than those of the beam ions, the evaporation residues radius is greater than that of the beam particles. The different trajectories allow a clear separation between the two types of particles, also for measurements performed at 0°. The electrostatic deflector is contained in a stainless steel cylinder 30 cm in diameter and 85 cm in length. Inside the cylinder two

pairs of stainless steel rectangular electrodes with smooth surface are placed. Each electrode has dimensions of 25 cm × 12 cm and a thickness of 0.5 cm. The distance between the plates is adjustable externally and separately for each electrode. Two different and independent field regions are generated, which allow a good adjustment for the different experimental conditions by minimizing the scattering of the beam on the plates. Two high voltage power supplies bring the electrodes up to a maximum voltage of around 40 kV and a collimator placed between the reaction chamber and the electrostatic deflector (entrance collimator) defines the acceptance angle of the deflector.
The applied voltage together with the geometry of the deflector plates bend slightly the primary beam that is stopped on a side of a collimator (exit collimator) placed at the end of the deflector. The ER, having lower electric rigidity, pass through the collimator and reach the detection system. The applied voltage is chosen for each energy to maximize the transmission of residues. But not all the beam particles are stopped, in typical fusion systems the rejection factor, defined as the ratio between the number of incoming and outgoing beam particles from the deflector, is $\sim 10^{7-8}$, according to the beam energy. Indeed, as a result of the scattering in the target and the multiple collisions with the electrodes or the edges of the collimators, a fraction of the beam particles, degraded in energy, enters the exit collimator. A further separation of the two types of ions is therefore necessary, which is realized by the detector telescope downstream of the exit collimator.

3.2 Detector telescope

The telescope discriminates the particles by exploiting the longer time of flight of more massive particles with respect to lighter particles of the same kinetic energy. This allows to distinguish the ER from the ions of the beam by measuring their TOF and their energy E. The telescope (Fig.3.4) consists of two microchannel plates detectors (MCP) [11], a ionization chamber (IC) [12] and a heavy-ion partially depleted silicon surface barrier detector inside the IC. Before reaching the silicon detector, the particles pass through an ionization chamber which provides their differential energy loss. In this configuration the silicon detector measures the residual energy. The telescope and the deflector are mounted on a platform which can be rotated in order to perform angular distribution measurements.

In order to calculate the TOF the use of MCP allow of detecting ions without significantly change their energy. They are based on pair of 43×63 mm^2 glass plates appropriately built to act as very compact electron multipliers with high gain (around 10^3 each plate). The ions do not interact directly with the plates, they pass through a carbon foil of about 20 μg/cm^2 placed perpendicularly to their direction. As result

of the interaction of the ions with carbon delta-electrons are emitted which are subsequently accelerated and bent onto the plates by an electrostatic mirror placed at 45°, where has been applied a voltage of about 1 kV. The produced signals are vary fast (around 2ns risetime) with a typical amplitude of tenths-hundreds of mV for heavy ions. Each MCP detector has a transparency of 85%, due to the presence of several grids, whereas their measured intrinsic efficiency is close to 100% for heavy ions.
The two MCPs yield the TOF together with the silicon detector, placed at the end of the telescope, that provides the starting signal for the TOF and triggered the data acquisition. The two flight bases are 666 mm and 1047 mm. The time resolution of the MCP detectors is comparable to that of the Silicon detector, and overall they sum up to around 300 ps.

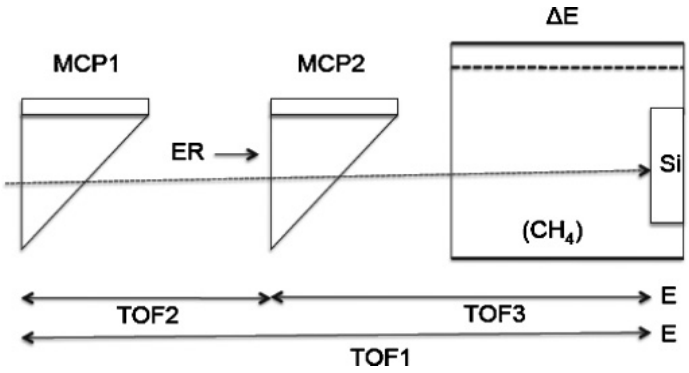

Figure 3.4: Scheme of detector telescope

The last detector of the telescope is a conventional ionization chamber using a Frisch grid shown schematically in Fig.3.5. The two parallel electrodes generate an electric field perpendicular to the beam line. The advantage of this transverse field ionization chamber is a fast separation of the formed ion pairs from the beam line. In addition, the Frisch grid removes the dependence of the anode pulse amplitude on the transverse position of the interaction. The cathode consists of one single plate of stainless steel, whereas the anode is segmented into three parts of 8 cm, 6 cm and 14 cm. This division of the anode allows to provide three differential energy loss signals (ΔE) which enable particle identification, however in this experiment the three signals were combined in a single one. The pressure was chosen so that the ER lose about half of their energy in the gas, and for this experiment has been initially set to 40 mbar and then reduced to 35.5 mbar for lower energies. The applied voltage chosen was 400 V in order to maximize the electron drift velocity. The gas used is methane CH_4, kept flowing during the measurements in order to assure its purity, despite the interactions with crossing ions and the impurities that may be produced by the walls and various components of the circuit. The gas flow also reduces the

recombination and assures a good energy resolution. At the end of the IC a circular (600 mm^2) silicon detector is placed, in order to measure the residual energy of the particles.

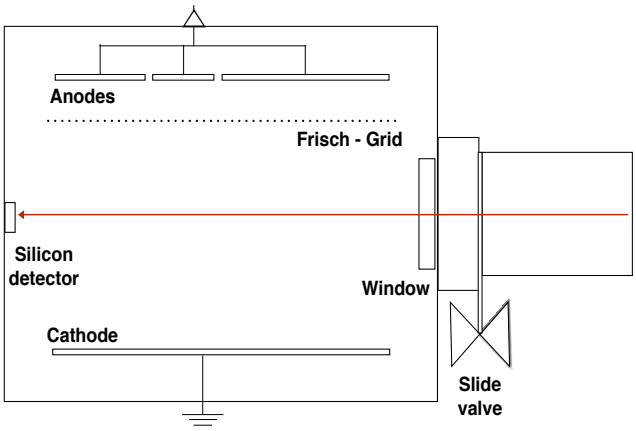

Figure 3.5: Scheme of ionization chamber with Frisch grid

3.3 Electronics and acquisition system

The scheme of the electronics used for processing the signals from the monitors, MCP, IC and Si detector is shown in Fig. 3.6. Most of the electronic chain is built up using standard NIM modules, due to the limited number of the parameters to be acquired and to the superior versatility of such kind of modules. The signals from each monitor is fed to the preamplifier which gives as outputs time and energy signals. The energy signals are connected to the inputs of a fast spectroscopy amplifier. Then, the signal is sent to a linear gate stretcher and processed by the ADC. The time signals follow a different way. First they are amplified with a fast amplifier and subsequently sent to a Constant Fraction Discriminator (CFD) module. The output signals of the CFD are sent to a gate generator and then to a logical unit, where the four monitor signals are put in OR with the time signal of the silicon detector placed in the IC. Each MCP provides a time signal. This signal is passed through a time pick-off pre-amplifier and fed into the CFD. The output signals of the CFDs are delayed and used as stop and/or start of the TAC module. Three TAC modules are currently in use providing three time of flight signals (TOF). Each TAC is started by the signal of the detector with lower rate, in order to prevent that the TAC receives signals not followed by a stop. Therefore, the signals of the MCP, conveniently delayed, provide the stop for the two TACs, measuring the time of flight between the first (second) MCP and the silicon detector, referred to as TOF1 (TOF3). Another TAC is employed to

measure the time of flight between the two MCP (TOF2). The signal from the silicon detector is fed to the pre-amplifier, then the energy signal is further amplified, sent to the linear gate stretcher and subsequently to the ADC. The time signal feeds a fast amplifier and subsequently a CFD. Two output signals of CFD are used as start of TOF1 and TOF3, while a third one is sent to the gate generator. The output of this gate generator is sent in logical OR with monitors and the output of the logic unit provides the trigger which enables the data acquisition. The ionization chamber with transverse field provides an energy signal which passes through a pre-amplifier and then is further amplified by a fast spectroscopy amplifier. The output feeds the linear gate and stretcher to be finally processed by the ADC.

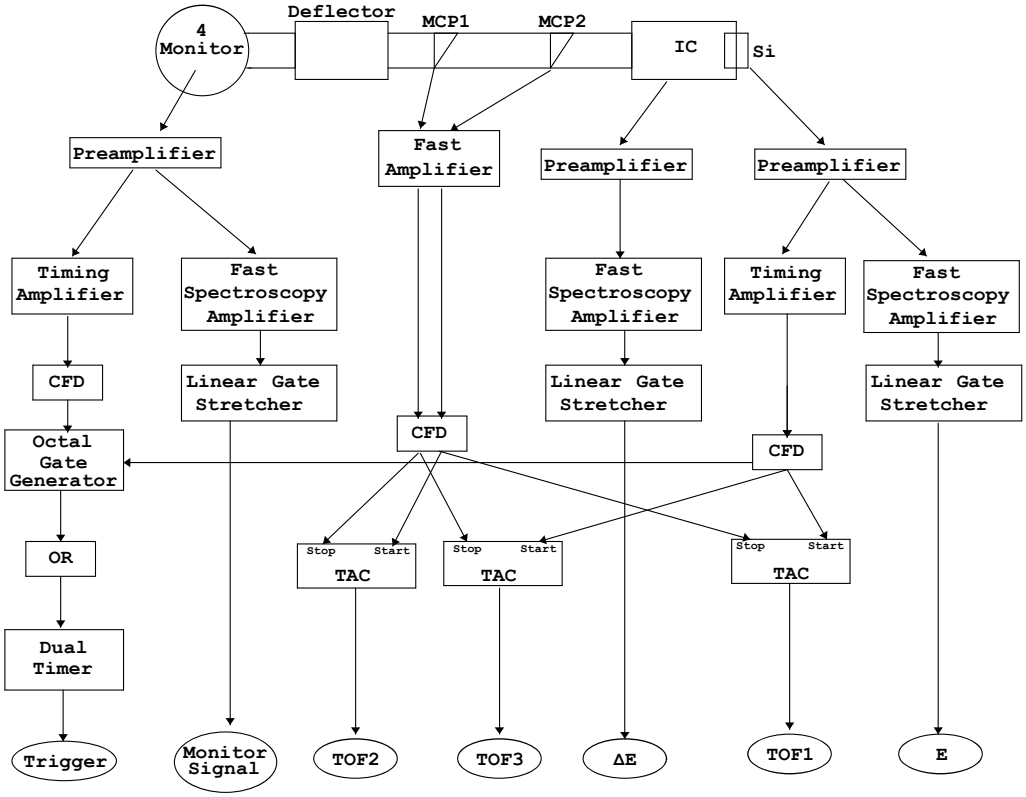

Figure 3.6: Scheme of the electronic chain of the set-up

Chapter 4

Data analysis

4.1 Experimental procedure

The experiment was designed to perform a detailed measurement of the fusion excitation function for the ^{58}Ni + ^{64}Ni system and was run for seven days. The XTU-Tandem accelerator provided the ^{58}Ni beam. The target consisted of 50 μg/cm^2 ^{64}Ni on a 20 μg/cm^2 carbon backing that introduced an average beam energy loss of around 1.25 – 1.31 MeV, which was taken into account in the analysis. The energies studied follow a previous experiment of Beckerman in the range E_{lab}=200.1 - 172.4 MeV and then, in order to measure smaller cross sections, the range E_{lab}=171.0 - 167.0 MeV was studied. The ^{64}Ni target were mounted on the six-position target holder. The energy was gradually changed starting from the highest value, in order to minimize hysteresis phenomena in the analyzing magnet placed at the exit of the accelerator. At every energy change the beam was refocused on the target using a quartz.

Fusion cross sections have been determined by direct detection of the fusion evaporation residues (ER) by separating them from the beam particles using the electrostatic deflector. The voltage applied to the electrodes was tuned during the experiment to maximize the number of ER detected after the deflector stage (yield of ER). The yield measurement was performed at the highest energy (200.1 MeV) and the maximum transmission was reached at the voltage of ±32.0 kV on each deflector electrode. For the other beam energies the applied voltage was scaled for the estimated electrical rigidity of the ER.

The ER were identified by a Time-of-Flight (TOF)–ΔE–Energy telescope composed of two micro-channel plate time detectors followed by the ionization chamber IC and by the silicon detector placed in the same gas (CH_4) volume of the IC. The silicon detector placed at the end of the detector telescope measured the residual energy of the ER and gave the start signal for the two TOF as well as the trigger for the data acquisition. The whole set-up was at first placed at an angle of 1° respect to the beam direction and then moved to angles of 2° and 1.5° for the lower energies,

in order to reduce the background of beam-like particles compared to the number of ER. Four silicon detectors placed in the reaction chamber symmetrically around the beam direction at the same scattering angle have been used to monitor the beam and to normalize the fusion yields to the Rutherford scattering cross section.

4.2 Total fusion cross section and excitation function

The telescope provides three times of flight TOF_1 (between the first MCP and the silicon detector),TOF_2 (between the two MCP) and TOF_3 (between the second MCP and the silicon detector), a total energy loss ΔE and a residual energy E. By correlating these variables, it is possible to identify the ER and estimate the total fusion cross sections. An example of TOF_3-E and TOF_3-ΔE matrices for different energies can be seen in Fig. 4.1 .

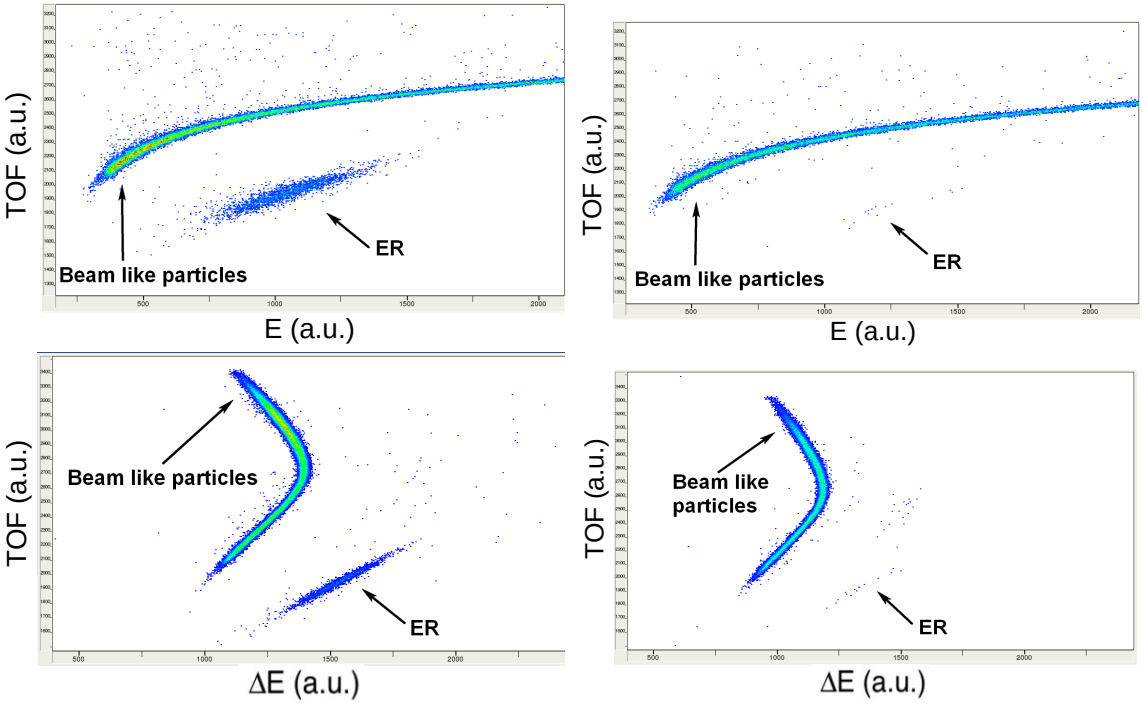

Figure 4.1: Example of TOF_3-E (upper panels) and TOF_3-ΔE (bottom panels) spectra for energies of 190.5 MeV, above the Coulomb barrier, (left) and of 171.0 Mev (right).

When the energy is far below the barrier, the number of ER compared to background events decreases rapidly. The identification of ER becomes therefore more

difficult and it is necessary to apply software conditions in order to remove the background, identifying the ER by using the various independent parameters (two TOF, ΔE and E) that are measured.

The four silicon detectors placed inside the reaction chamber detected the beam ions which scattered on the target, at an angle of 16.05° with respect to the beam direction. Examples of the spectra provided by the four monitors at the energy of 171.0 MeV are shown in the Fig. 4.2. These spectra allow to estimate the Rutherford cross section, which is used to normalize the fusion cross section. This normalization allows to correct also for the variations of beam parameters that may change during long data acquisitions.

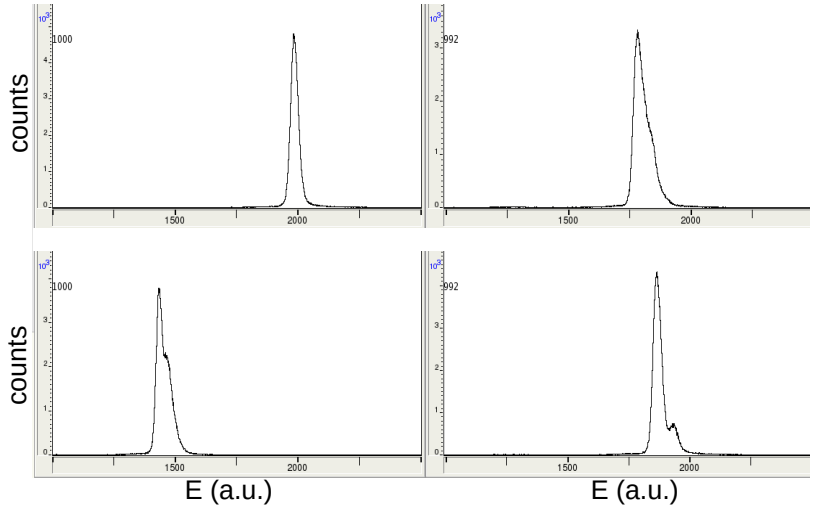

Figure 4.2: Examples of the spectra provided by the four monitors for the energy of 171.0 MeV

The ER angular distribution was also measured at the E_{lab}=190.5 MeV in order to obtain the total fusion cross section. The differential cross section can be obtained from the ER and monitors count by this formula:

$$\frac{d\sigma^f}{d\Omega}(E,\theta) = \frac{d\sigma^{Ruth}}{d\Omega}(E,\theta_{lab})\frac{N_{ER}}{N_{mon}}\frac{\Delta\Omega_{mon}}{\Delta\Omega_{ER}}\frac{1}{\varepsilon}$$

where, N_{mon} is the number of elastic scattering events detected by the monitors, $\Delta\Omega_{mon}$ is the total solid angle subtended by them and θ_{lab} is the monitor angle 16.05°. N_{ER} is the number of ER counted by the silicon detector and $\Delta\Omega_{ER}$ is its solid angle. The quantity ε can be explicitly expressed as the product of the deflector transmission T=0.74$\pm$0.03 and the telescope transparency. The value of T was estimated on the basis of an interpolation between the transmissions determined in past years for several different systems. T does not essentially depend on the

energy, however it is a function of the mass asymmetry of the system under study. The total fusion cross section for each energy can be obtained by the formula

$$\sigma_f = K(E)\frac{d\sigma^f}{d\Omega}(E,\theta)$$

where the parameter K(E) is a quantity weakly dependent on the energy and can be extracted from the angular distribution. However since $\frac{d\sigma^{Ruth}}{d\Omega}(E,\theta_{lab}) = A(\theta_{lab})\frac{1}{E^2}$, with θ_{lab} fixed, and K(E)=K constant the quantity $\frac{N_{ER}}{N_{Ruth}}\frac{1}{E^2}$ is proportional to the fusion cross-section with the same constant for each energy, therefore this quantity can be normalized to the cross section measured in a previous experiment for the same system [13] for the highest energy and then obtain the total fusion cross section at all measured energies. The obtained values are reported in the Table 4.1, and compared with the Beckerman's data (Fig. 4.3)

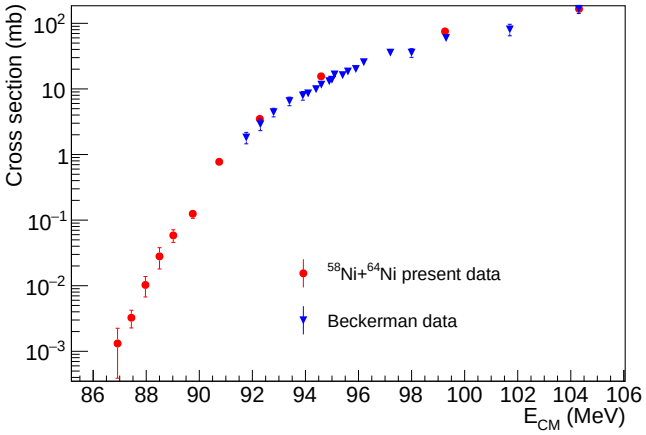

Figure 4.3: Comparison between excitation function obtained in this experiment and in the Beckerman experiment for the system ^{58}Ni + ^{64}Ni

Only the statistical uncertainties were considered and the distribution of the particles counts is Poissonian so that the associated uncertainty is $\sqrt{N}$. The cross sections vary of five orders of magnitude in the energy range considered for the measurements.

4.3 Astrophysical S-factor and logarithmic slope

A first approach to verify the presence of hindrance consists in the calculation of the Logarithmic derivative L(E) and the Astrophysical S factor S(E). The definition of the logarithmic derivative is

$$L(E) = \frac{dln(E\sigma)}{dE}$$

E_{CM}	σ_f	$\Delta\ \sigma_f$
104.31	166	2
99.26	75.3	1.4
94.59	15.6	0.2
92.28	3.50	0.10
90.75	0.77	0.05
89.76	0.12	0.02
89.02	0.06	0.01
88.50	0.03	0.01
87.97	0.010	0.003
87.44	0.0032	0.0010
86.92	0.0013	0.0009

Table 4.1: Cross sections measured in this experiment for the system ^{58}Ni + ^{64}Ni, the quoted errors are statistical uncertainties (see text)

that can be obtained from the experimental data using the incremental ratio:

$$L(E) = \frac{ln(E_2\sigma_2) - ln(E_1\sigma_1)}{E_2 - E_1}$$

The statistical uncertainty associated with the logarithmic derivative is estimated as the propagation of the statistical uncertainty of the cross section. The results are shown in Fig. 4.4 where the value of $L_{CS} = \frac{\pi\eta}{E}$ is also plotted.

From this plot it can be seen that the experimental value of L(E) is always below the L_{CS} value, so that no maximum for the astrophysical S factor is expected.

Also the astrophysical S factor has been calculated from the cross section values by the formula:

$$S(E) = E\sigma(E)e^{2\pi(\eta-\eta_0)}$$

The value η_0 is used as a normalization factor to obtain S(E) in a reasonable range of values.In this case $\eta_0 = 69.3$ has been used. As for the logarithmic derivative the statistical uncertainty for S(E) is estimated by propagating the statistical errors on the cross sections. The results are shown in Fig. 4.5. It can be seen that there is no maximum for S(E), as expected from the trend of L(E). The behavior of the logarithmic derivative and the astrophysical factor is a first evidence of the absence of hindrance in the ^{58}Ni + ^{64}Ni system. However to correctly understand the experimental results, a theoretical interpretation is necessary. In this thesis a coupled-channels analysis was performed using the CCFULL code.

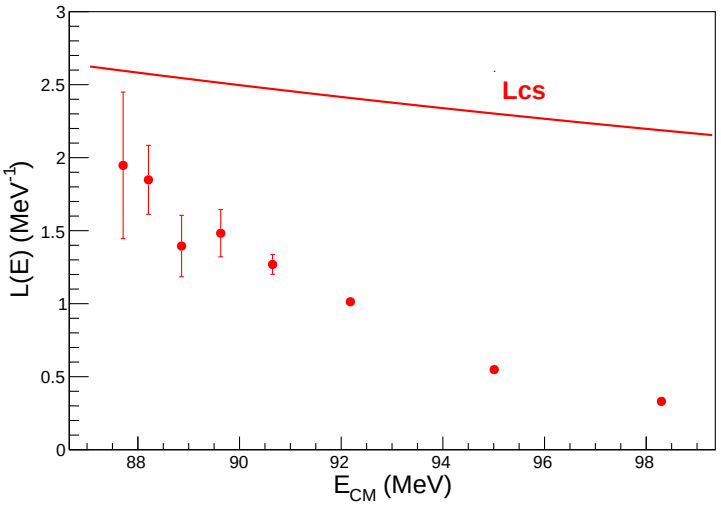

Figure 4.4: Logarithmic derivative for the system ^{58}Ni + ^{64}Ni. the L_{CS} line is defined in the text

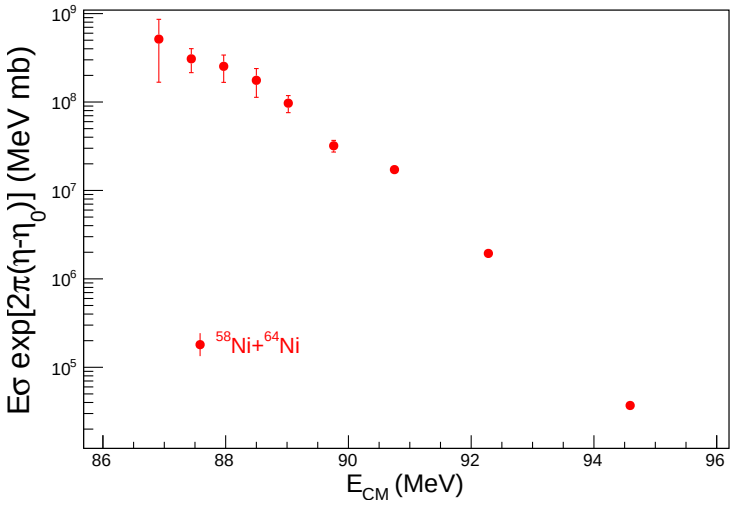

Figure 4.5: Astrophysical S factor for the system ^{58}Ni + ^{64}Ni

Chapter 5

Comparison with CC calculations

The experimental data of the fusion reactions have been compared to the theoretical calculations based on the coupled-channels model. The comparison is of great importance from a structural point of view, in order to verify the effect of the excited states involved in the fusion dynamics. The CC calculations were performed by means of the CCFULL code [14], which solves the coupled equations by employing the isocentrifugal approximation and the incoming wave boundary condition. The energies of the excited states of both target and projectile nuclei, as well as the associated deformation parameters, are given in Table 5.1. The deformation parameters for each state has been obtained from the literature [15] [16]. The parameters obtained for the Akyüz-Winther potential are reported in Table 5.2.

Nucleus	E(MeV)	λ^{π}	β_{λ}
^{58}Ni	1.454	2^+	0.18
	4.475	3^-	0.20
^{64}Ni	1.346	2^+	0.18
	3.560	3^-	0.19

Table 5.1: Nuclear structure parameters for CCFULL calculations

V_0 (MeV)	r_0 (fm)	a_0 (fm)	V_b (Mev)	R_b (fm)
73.87	1.18	0.67	97.6	10.75

Table 5.2: Well depth V_0, radius r_0 and diffusivity a_0 of the Akyüz-Winther potential and the resulting height V_b, and the position R_b of the Coulomb barrier for the system ^{58}Ni+^{64}Ni.

5.1 CC prediction and the effect of the transfer channel couplings

The resulting fusion cross section overestimate the experimental data (Fig. 5.1 left) above the Coulomb barrier. This effect may be caused by an underestimation of the Coulomb barrier by the Akyüz-Winther potential. In order to correct for this effect the barrier height has been modified to V_b=99.3 MeV, and following this modification the the well depth of the nuclear potential has to be V_0=138.0 MeV and the radius is r_0=1.10 fm, with the same a_0=0.67 fm.

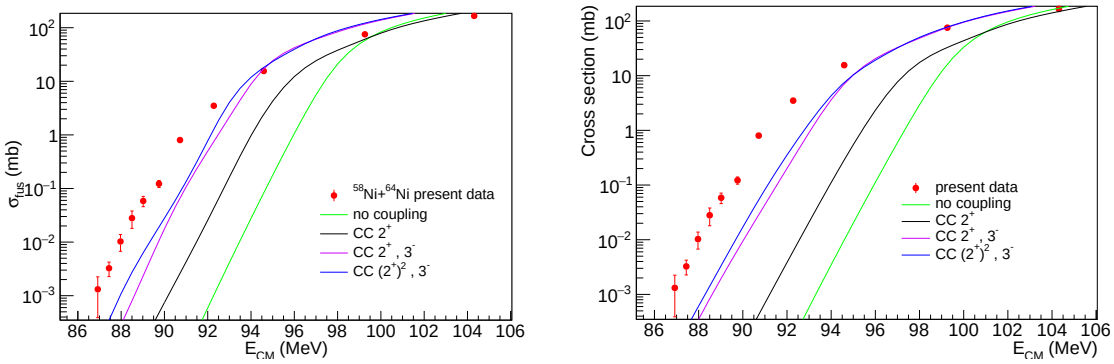

Figure 5.1: CC calculation of the excitation function for the system ^{58}Ni + ^{64}Ni with Akyüz-Winther potential (left panel). CC calculation of the excitation function for the system ^{58}Ni + ^{64}Ni with a modified Akyüz-Winther potential (right panel).

The resulting calculation is shown in Fig. 5.1 right, the couplings lead to a large enhancement of the fusion below the barrier with respect to the no coupling limit, but the result still underestimates the cross sections at low energies, so that there is no evidence of hindrance for this system. This effect may be attributed to the presence of neutron transfer channels with positive Q-value. The CCFULL code allows to include the pair-transfer between the ground states of the interacting nuclei through the schematic form factor

$$F_{trans}(r) = F_t \frac{dV_N^{(0)}}{dr}$$

The Q-value for this reaction is Q=3.89 MeV, the coupling strength F_t best fitting the data is F_t=0.6 MeV. With the introduction of the transfer channel the resulting fusion cross section underestimates the experimental data above the Coulomb barrier, so the barrier height has been further modified to V_b=98.63 MeV (V_0=151.85 MeV, r_0=1.10 fm and a_0=0.67 fm). The results including both the inelastic and transfer couplings are in good agreement with the experimental data as shown in Fig. 5.2.

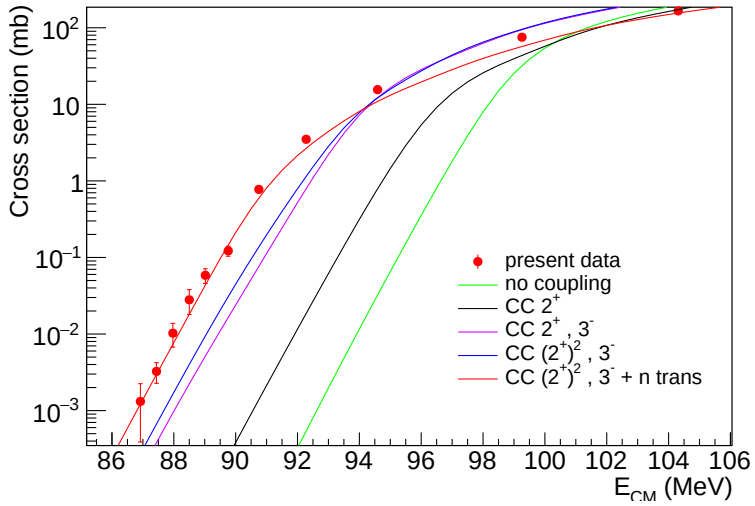

Figure 5.2: CC calculations of the excitation function for the system ^{58}Ni + ^{64}Ni taking in to account also the transfer channel.

Also the logarithmic derivative (Fig. 5.3) and the astrophysical S factor (Fig. 5.4) has been calculated. As expected the experimental value of the logarithmic derivative remains always lower than the L_{CS} line and consequently there is no maximum for the astrophysical S factor.

The fusion Q-value for this system is negative, then the cross section for energies lower than the E=-Q have to be zero. For this reason the astrophysical S factor has to develop a maximum at some energy above -Q. However the presence of the transfer channels results in a shift of the onset of the hindrance effect towards low energies.

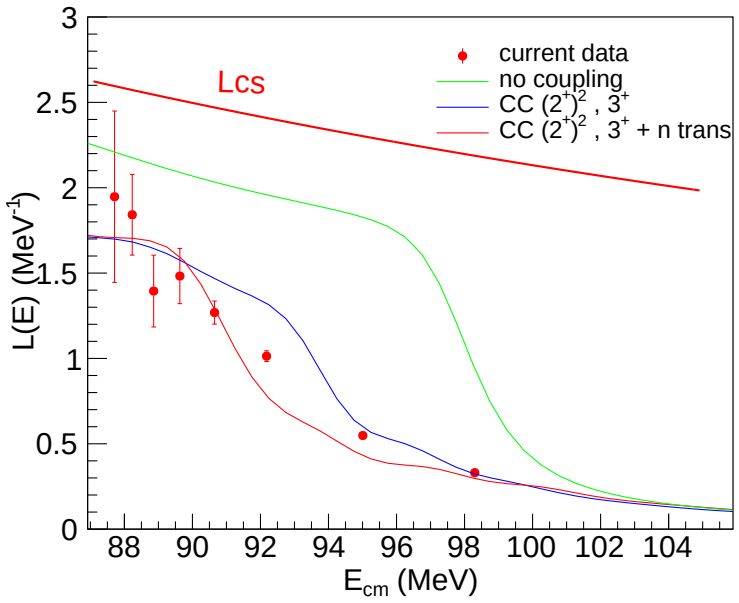

Figure 5.3: CC calculations of the logarithmic derivative for the system ^{58}Ni + ^{64}Ni.

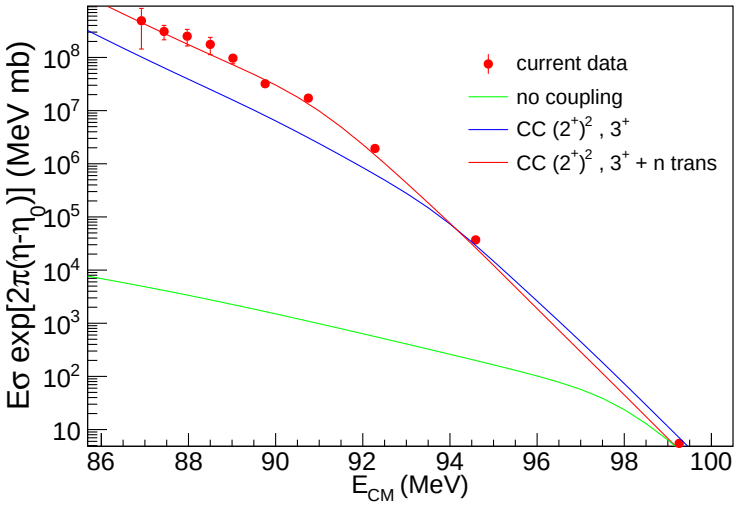

Figure 5.4: CC calculations of the astrophysical S factor for the system ^{58}Ni + ^{64}Ni.

5.2 Behavior of near-by system: ^{64}Ni+^{64}Ni

The behavior of the ^{64}Ni+^{64}Ni system has been also studied using the Jiang experimental data and performing the CC calculation using a modified Akyüz-Winther potential (V_0=127.92 MeV, r_0=1.12 fm and a_0=0.68 fm). The results obtained are shown in Fig. 5.5 where can be seen that the theoretical prediction overestimate the experimental data, so there is evidence of hindrance effect.

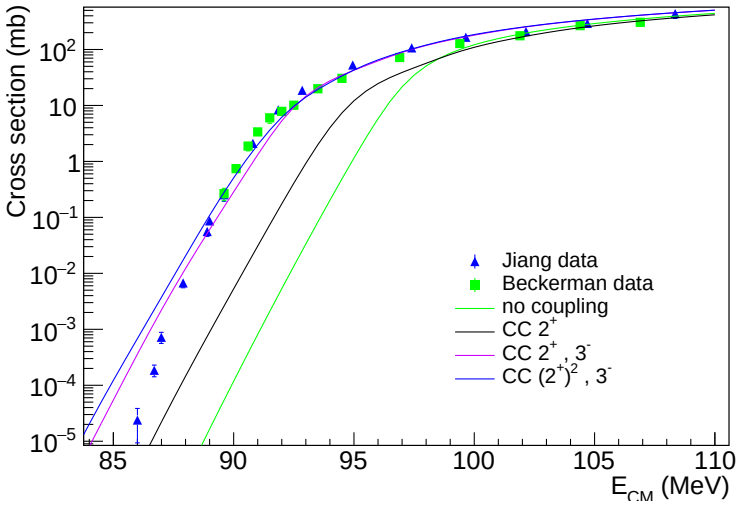

Figure 5.5: CC calculations of the excitation function for the system ^{64}Ni + ^{64}Ni

Also the logarithmic derivative (Fig. 5.6) and the astrophysical S factor (Fig. 5.7) have been obtained. The slope for this system keeps increasing, reaches and overcomes the value L_{CS}. Consequently, a S maximum develops with decreasing energy.

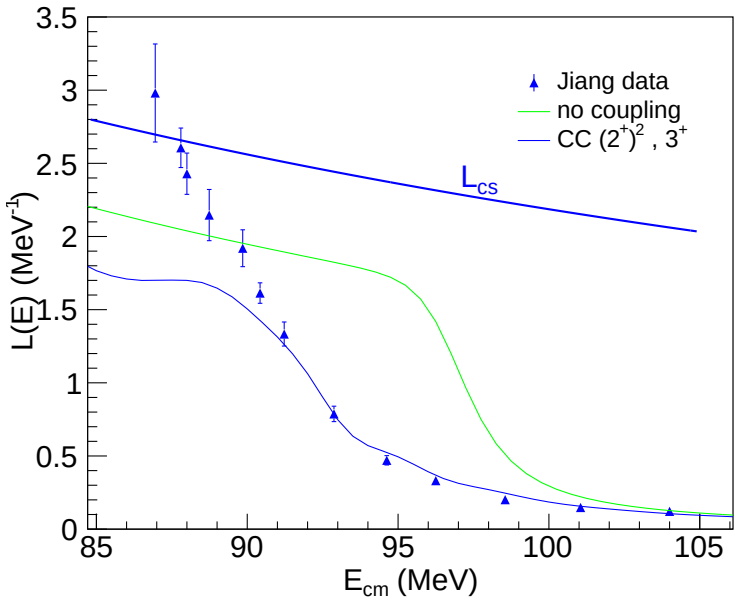

Figure 5.6: CC calculations of the logarithmic derivative for the system ^{64}Ni + ^{64}Ni

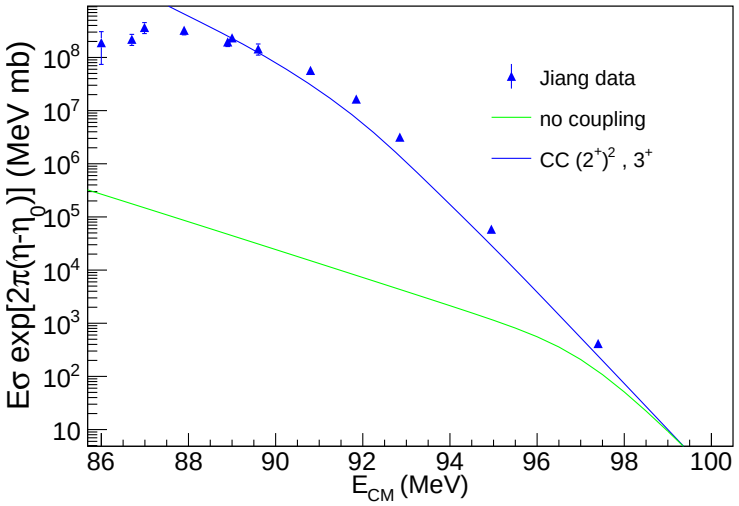

Figure 5.7: CC calculations of the astrophysical S factor for the system ^{64}Ni + ^{64}Ni

A comparison of the excitation function of the ^{58}Ni + ^{64}Ni and the ^{64}Ni + ^{64}Ni systems was made as shown in Fig. 5.8 where the cross sections are plotted in a reduced energy scale (E/Vb) so to correct for the different Coulomb barriers of the two systems.

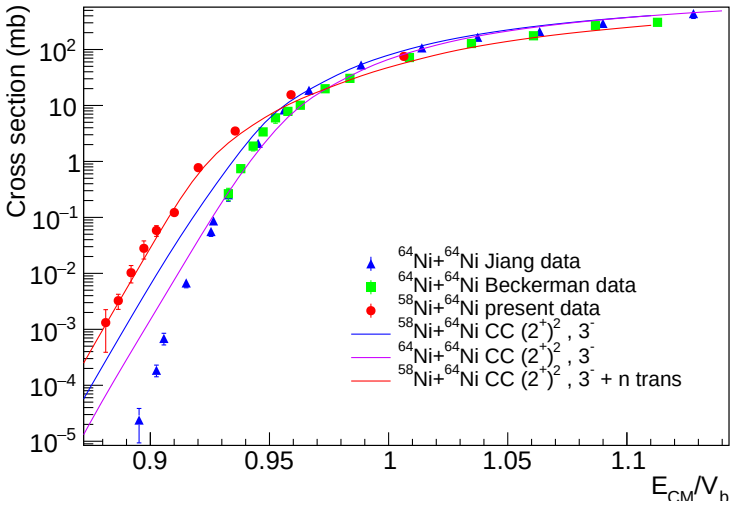

Figure 5.8: Comparison of the excitation function between the ^{58}Ni + ^{64}Ni and the ^{64}Ni + ^{64}Ni systems.

The logarithmic derivative (Fig. 5.9) and the astrophysical S factor (Fig. 5.10) have also been compared between the two systems.

In these plots we can see their different behavior for energies below the Coulomb barrier.

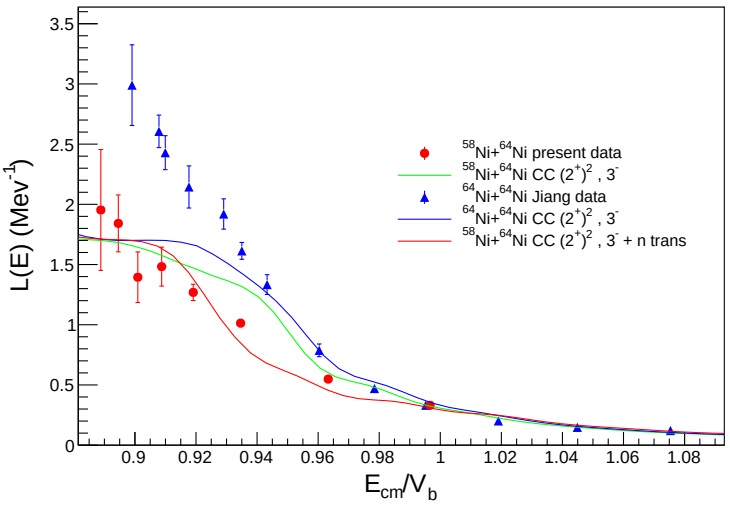

Figure 5.9: Comparison of the logarithmic derivative between the ^{58}Ni + ^{64}Ni and the ^{64}Ni + ^{64}Ni systems.

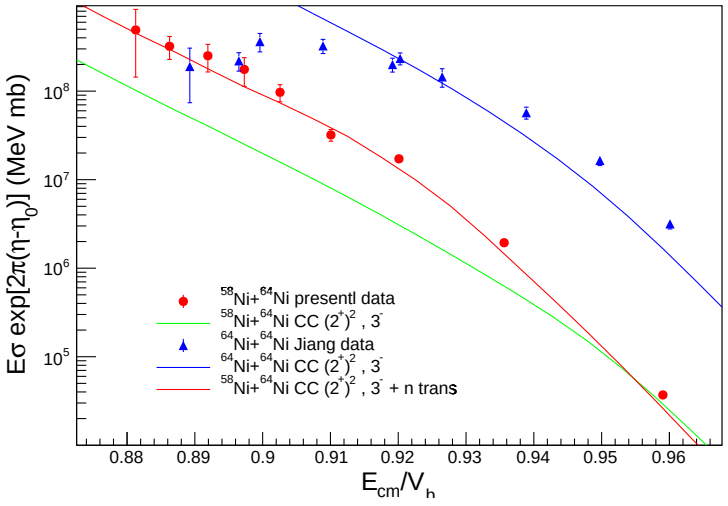

Figure 5.10: Comparison of the astrophysical S factor between the ^{58}Ni + ^{64}Ni and the ^{64}Ni + ^{64}Ni systems.

5.3 Another similar case: ^{96}Zr+^{40}Ca

Another similar case to ^{58}Ni + ^{64}Ni is the ^{40}Ca+^{96}Zr system which also presents transfer channels with positive Q-value. Also in this case the CC calculations underestimate the obtained cross-section below the the Coulomb barrier as shown in Fig. 5.11 (left).

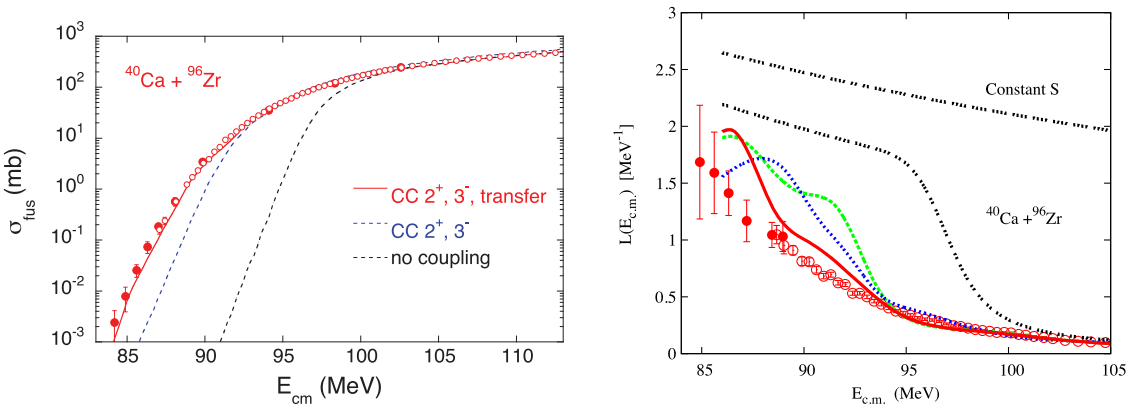

Figure 5.11: Excitation function for the ^{40}Ca + ^{96}Zr (left panel), Logarithmic derivative for ^{40}Ca + ^{96}Zr and theoretical prediction for unidimensional model (black dashed line), coupled-channel model involving one phonon of the 2^+ excited states (green dashed line),one phonon of the 2^+ and one of the 3^- excited states (blue dashed line) and two phonon of the 2^+ excited states and one of the 3^- excited states (red line) (right panel).

The CC calculations including the neutron transfer channels reproduce well the experimental data down to the lowest measured energies.

Also the logarithmic derivative (Fig. 5.11(right)) has been calculated where we can see that, as expected, the slope increases slowly and remains very low with respect to the constant S factor value.

Chapter 6

Summary and conclusion

In conclusion, in this thesis work the fusion reaction ^{58}Ni+^{64}Ni has been investigated by performing an experiment at XTU Tandem of Laboratori Nazionali di Legnaro. The set up using an electrostatic deflector and a detector telescope, for the separation of the fusion evaporation products from the beam particles, has been employed. In this way fusion cross sections have been measured in a wide energy range from above down to far below the barrier reaching a minimum cross section of about 1μb. The data have been compared with the CC calculations, showing that the theoretical predictions including two phonon of the 2^+ state and one of the 3^- state strongly underestimate the experimental cross section below the Coulomb barrier and there is a clear need for additional couplings. Including also the two neutron transfer channels the theoretical prediction is in good agreement with the experimental data. The logarithmic derivative and the astrophysical S factor have been extracted from the data. The logarithmic slope increases slowly and doesn't reach the constant S factor value, so that there no evidence for the hindrance phenomenon. This shows how the presence of neutron transfer channels with positive Q-value enhances the fusion cross section at low energies. What we have seen is similar to the case of ^{40}Ca + ^{96}Zr where the transfer channels with positive Q-value are also present. The obtained results has been compared with the ^{64}Ni+^{64}Ni system that presents a similar nuclear structure but doesn't have transfer channels with positive Q-value, and in this system the hindrance effect is observed. The behaviour of ^{58}Ni+^{64}Ni at deep sub-barrier energies is a strong experimental evidence of the validity of the recent suggestion that the availability of several states following transfer with Q>0, effectively counterbalances the repulsion caused by the Pauli exclusion principle [17].

Chapter 7

Appendix: Table of experimental data

Angle	$\frac{N_{ER}}{N_{mon}E^2}$	$\Delta \frac{N_{ER}}{N_{mon}E^2}$
1°	10.3	0.3
1.5°	8.0	0.3
2°	5.04	0.3
3°	1.54	0.7

Table 7.1: Angular distribution data at the energy of 190.5 MeV.

E_{CM} (Mev)	L(E) (MeV^{-1})	Δ L(E) (MeV^{-1})
98.3	0.331	0.003
95.01	0.549	0.008
92.18	1.01	0.03
90.65	1.27	0.07
89.63	1.5	0.2
88.86	1.4	0.2
88.23	1.8	0.2
87.71	1.9	0.5

Table 7.2: Logarithmic derivative obtained from experimental data.

E_{CM} (Mev)	S(E) (MeV mb)	Δ S(E) (MeV mb)
99.26	5.5	0.1
94.59	$3.70\ 10^4$	$5\ 10^2$
92.28	$1.94\ 10^6$	$5\ 10^4$
90.75	$1.7\ 10^7$	$1\ 10^6$
89.76	$3.2\ 10^7$	$5\ 10^6$
89.02	$1.0\ 10^8$	$2\ 10^7$
88.50	$1.8\ 10^8$	$6\ 10^7$
87.71	$2.5\ 10^8$	$9\ 10^7$
87.44	$3.1\ 10^8$	$9\ 10^7$
86.92	$5\ 10^8$	$3\ 10^8$

Table 7.3: Astrophysical S factor obtained from experimental excitation function using the scale factor $e^{2\pi\eta_0}$ where η_0=69.3 (see text).

Bibliography

[1] C. Y. Wong. "Interaction barrier in charged-particle nuclear reactions". In: *Physical Review Letters* 31.12 (1973), pp. 766–769.

[2] P.H. Stelson N. Rowley G.R. Satchler. In: *Phys. Lett. B* 254 (1991).

[3] C.L. Jiang et al. In: *Phys. Rev. Lett.* 89 (2002).

[4] C.H. Dasso R.A. Broglia. In: *Phys. Rev. C* 27 (1983).

[5] S.Misicu and H. Esbensen. "The large-area micro-channel plate entrance detector of the heavy-ion magnetic spectrometer PRISMA". In: *Phys. Rev. Lett.* 96,112701 (2006).

[6] Ö. Akyüz and A. Winther. "Nuclear Structure and Heavy-Ion Collisions". In: *Proc. Int. School of Physics "Enrico Fermi" Course LXXVII, Varenna* (1979).

[7] S. Landowne C. H. Dasso and A. Winther. "Channel-coupling effects in heavy-ion fusion reactions". In: *Nuclear Physics A* 405 (1983), pp. 381–396.

[8] S. Landowne C. H. Dasso and A. Winther. "Barrier penetration in the presence of coupling to intrinsic degrees of freedom". In: *Nuclear Physics A* 432 (1985), pp. 495–513.

[9] K. Hagino and N. Takigawa. "Subbarrier fusion reactions and many-particle quantum tunneling". In: *128.6* (2012).

[10] G. Montagnoli A.M. Stefanini. "Fusion of ^{40}Ca + ^{96}Zr revisited: Transfer couplings and hindrance far below the barrier". In: *Physics Letters B* 728 (2014), pp. 639–644.

[11] G. Montagnoli et al. "The large-area micro-channel plate entrance detector of the heavy-ion magnetic spectrometer PRISMA". In: *Nuclear Instruments and Methods in Physics Research* 547.2-3 (2005), pp. 455–463.

[12] H. W. Fulbright. "Ionization Chambers". In: *Nuclear Instruments and Methods* 162 (1979), pp. 21–28.

[13] M. Beckerman et al. "Sub-barrier fusion of $^{58'64}$Ni with ^{64}Ni and ^{74}Ge". In: *Physical Review C* 2 (1982), pp. 838–849.

[14] N. Rowley K. Hagino and A. T. Kruppa. “A program for coupled-channels calculations with all order couplings for heavy-ion fusion reactions”. In: *Computer Physics Communications* 123 (1999).

[15] S. RAMAN. “Transition probability from the ground to the first exited 2^+ state of even-even nuclides”. In: *Atomic Data and Nuclear Data Tables* 78 (2001), pp. 1–128.

[16] T. KIBEDI and R. H. SPEAR. “Reduced electric-octupole transition probabilities, B(E3; 0_1^+ 3_1^-)—an update”. In: *Atomic Data and Nuclear Data Tables* 80 (2002), pp. 35–82.

[17] C. Simenel et al. In: *Phys. Rev. C* 95 031601(R) (2017).